Immunological profiles in Lynch syndrome colorectal cancers are not specific to mismatch repair gene defects

Noah C. Helderman[a], Marieke E. IJsselsteijn[b], Madalina Cabuta[a], Manon van der Ploeg[b], Tom van Wezel[b], Aysel Ahadova[c], Matthias Kloor[c], Hans Morreau[b], Maartje Nielsen[a]*, Noel F.C.C. de Miranda[b]*

*shared last authors

[a]Department of Clinical Genetics, Leiden University Medical Center, Leiden, The Netherlands

[b]Department of Pathology, Leiden University Medical Center, Leiden, The Netherlands

[c]Department of Applied Tumor Biology, Heidelberg University Hospital, Clinical Cooperation Unit Applied Tumor Biology, German Cancer Research Centre (DKFZ), Heidelberg, Germany.

Abbreviations

β2M, β2-microglobulin; CRC, colorectal cancer; FFPE, formalin-fixed, paraffin-embedded; GZMB, granzyme B; HLA, Human Leukocyte Antigen; IHC, immunohistochemistry; IMC, imaging mass cytometry; IQR, interquartile range; LS, Lynch syndrome; mIF, multiplex immunofluorescence; *MLH1*-PM, *MLH1* promotor hypermethylation; MMR, mismatch repair; MMR-d, mismatch repair-deficiency; MSI, microsatellite instability; PD-(L)1, programmed death(-ligand) 1; SD, standard deviation.

Correspondence

Noel F.C.C. de Miranda (N.F.de_Miranda@lumc.nl), Department of Pathology, Leiden University Medical Center, Leiden, The Netherlands

Acknowledgments

The authors sincerely thank all patients and their families for participating in this study. We gratefully acknowledge the PALGA-group collaborators/participating pathology centers for providing patient samples; T.C.T.E.F. Cronenburg for assisting in the identification of tumor regions of interest; S. van Oost for assisting in the data analysis; and R. van der Breggen for technical assistance.

Abstract

Background and aims: Colorectal carcinomas (CRCs) in patients with Lynch syndrome (LS) exhibit heightened immunogenicity due to mismatch repair deficiency (MMR-d), often resulting in favorable responses to T cell immune checkpoint therapies. Recent studies indicate that the phenotype and genotype of LS-associated CRCs vary depending on the specific MMR gene mutated. Here, we investigated whether the immune profiles of LS-associated CRCs differ based on the MMR gene defects. **Methods:** Tissue material from 18 *MLH1-,* 16 *MSH2-,* 40 *MSH6-, and* 23 *PMS2*-mutated CRCs and 35 sporadic MMR-d CRCs were included in the study. Imaging mass cytometry (IMC) analysis, along with targeted multiplex immunofluorescence imaging (mIF) and immunohistochemistry, were applied to examine the tumor immune microenvironment, including Human Leukocyte Antigen (HLA) class I and programmed death-ligand 1 (PD-L1) expression. **Results:** Unsupervised hierarchical clustering of cell phenotypes identified by IMC, followed by mIF validation, revealed comparable lymphoid and myeloid cell infiltration levels across CRCs from all MMR groups. Infiltrating T cell levels negatively correlated with the number of mutations at coding microsatellite sequences, particularly in *MLH1*-mutated CRCs. HLA class I defects were observed in 76% of all CRCs. These defects were more frequently accompanied by β2M defects in hereditary MMR-d CRCs (67%) compared to sporadic MMR-d CRCs (37%), and did not associate with the number of γδ T cells, which were present in CRCs from all MMR groups. PD-L1 expression in tumor cells was only detected in 8% of all CRCs. **Conclusion:** Our findings illustrate that, from an immunological perspective, there is no evidence of differing immunogenic features across MMR defects. This is important to consider when developing preventive vaccine strategies and evaluating immunotherapy for LS patients and those with MMR-d CRCs.

Keywords: colorectal cancer; genetics; immunology; immunotherapy; Lynch syndrome; mismatch repair

Introduction

Lynch syndrome (LS) is recognized as one of the most prevalent inherited cancer syndromes, primarily conferring a predisposition to colorectal cancer (CRC) and endometrial cancer. It arises in carriers of pathogenic variants in one of the mismatch repair (MMR) genes, including *MLH1* (OMIM #609310), *MSH2* (OMIM #120435), *MSH6* (OMIM #614350), and *PMS2* (OMIM #614337), or more rarely from an *EPCAM* (OMIM #613244) deletion that lies upstream of *MSH2*.[1]

In general, CRCs from LS patients are highly immunogenic due to the widespread accumulation of mutations, particularly nucleotide insertions and deletions at microsatellite sequences, due to MMR deficiency (MMR-d).[1] Insertions and deletions in the coding genome are thought to be particularly immunogenic due to the generation of frameshift proteins that are new to the host's immune system and, therefore, evoke anti-tumor immune reactivity.[2]

The remarkable immunogenicity of LS-associated CRCs is evident through pronounced infiltration of (cytotoxic) T cells, the frequent observation of immune evasion events, and immune cell reactivity to frameshift proteins in LS-associated CRCs.[3-14] Capitalizing on this, patients with LS-associated CRCs or sporadic MMR-d CRCs generally respond better to immune checkpoint blockade than those with MMR-proficient CRCs.[15-19] Furthermore, this population may benefit from preventive cancer vaccine development, as certain frameshift proteins are shared across most MMR-d CRCs due to the positive selection of underlying driver mutations. [20, 21]

Recent studies demonstrated that LS presents as a highly heterogeneous disease, encompassing variation in both phenotypic aspects such as CRC risks[22-30], and genotypic factors, including the type of somatic mutations (e.g., single-nucleotide variants, insertions, deletions) and the genes affected by these mutations.[31-37] These disparities are likely influenced by the underlying MMR defect, among other contributing factors, and have prompted whether LS should be redefined as a collection of distinct gene-related syndromes.[38, 39]

We recently observed a reduced frequency of MMR-d signature-associated insertion and deletion mutations in *MSH6*-mutated CRCs compared to other LS-associated CRCs.[36, 37] Given that these mutations typically underlie the observed immune responses in CRCs, our goal was to conduct a comprehensive characterization of the immune profiles in LS-associated CRCs to determine whether those are influenced by specific MMR gene defects.

Methods

Ethical statement

The Medical Ethical Committee of Leiden, The Hague, Delft (protocol P17.098) approved this study. Patient samples were managed in accordance with medical ethical guidelines outlined in the Code of Conduct for the responsible use of human tissue in the context of health research, as established by the Federation of Dutch Medical Scientific Societies. Informed consent was obtained from patients to utilize both tissue and data. Patients or the public were not involved in the design, or conduct, or reporting, or dissemination plans of our research

Patients and samples

Coded or anonymized formalin-fixed, paraffin-embedded (FFPE) tumor tissue blocks were obtained from the Department of Pathology of the Leiden University Medical Centre (Leiden, The Netherlands) and via the Dutch Pathology Registry (PALGA; reference LZV2022-68), respectively. The tumor tissue that was included originated from CRCs of 18 *MLH1*, 16 *MSH2*, 40 *MSH6*, and 23 *PMS2* variant carriers. Moreover, tumor tissue blocks from 35 patients with sporadic MMR-d CRC due to *MLH1* promotor hypermethylation (*MLH1*-PM) were included. Clinical and molecular characteristics of patients and samples were obtained from pathology reports and patient records.

Immunohistochemistry

See **Supplementary Table 1** for providers and relevant (user) details of all materials used in this study, including antibody clones.

Immunodetection. FFPE tumor tissue blocks were cut into 4µm sections and placed on silane-coated glass slides (VWR, Radnor, PA, USA). Immunohistochemical (IHC) detection of human leukocyte antigen (HLA) class I [HCA2 and HC10 clones], β2-microglobulin (β2M) [EPR21752-214 clone], programmed death-ligand 1 (PD-L1) [E1L3N clone] , and TCR δ [H-41], was performed as described previously.[10] In short, tissue sections were deparaffinized and rehydrated using xylene and decreasing ethanol concentrations, respectively. Endogenous peroxidase was blocked using 0.3% hydrogen/peroxidase methanol solution (Merck Millipore, Burlington, MA, USA) and heat-mediated antigen retrieval was achieved by boiling the sections in either sodium-citrate (0.1M, pH 6) or Tris-

EDTA (10/1mM, pH 9) buffer, following which the sections were cooled and incubated overnight with a primary antibody (**Supplementary Table 1**). Primary antibody binding was detected through incubation with BrightVision poly-horseradish peroxidase solution (Immunologic, Duiven, The Netherlands) and DAB+ chromogen (DAKO, Agilent Technologies, Santa Clara, CA, USA). Sections were counterstained with hematoxylin (Thermo Fisher Scientific, Waltham, MA, USA).

Scoring and quantitative analysis. An internal positive control (stromal cell staining) was used to score HLA class I, β2M, and PD-L1 expression in tumor cells (**Supplementary Figure 1**). Negative controls comprised 4µm tonsil tissue incubated with 1% bovine serum albumin (BSA)/PBS solution instead of primary antibodies during the procedure.

Quantitative analysis of γδ T cells in whole slide scans of tumor tissue was carried out using QuPath v0.4.3.[40] Initially, cell segmentation was performed utilizing Hematoxylin staining to identify cell nuclei. Subsequently, the positivity of the TCR V γ 3 marker in the cells was determined based on DAB intensity. Normalization was conducted to account for tissue area variations, and the resulting cell counts were reported as cells/mm².

Imaging mass cytometry

To identify immune cell phenotypes of interest, we applied a 40-marker IMC panel that has previously been designed and optimized[41], on eight tumors per MMR group. This approach allowed the analysis of both immune cell frequencies and the spatial context of immune cells. Antibody-metal conjugation, IMC immunodetection/acquisition, and downstream data analyses were performed as described previously by our group and will be summarized.[41-43]

Metal conjugation of antibodies. Conjugation of carrier-free IgG antibodies to purified lanthanide metals was performed using the Maxpar antibody labeling kit (Fluidigm, San Francisco, CA, USA), following which antibodies were eluted in 50µL antibody stabilizer solution (Candor Bioscience, Wangen im Allgäu, Germany) with 0,05% sodium azide and 50µl W-buffer (Fluidigm). Antibody

performance after conjugation was assessed by IHC on 4µm tonsil tissue. The marker panel included lineage, functional/activation, and structural markers (**Supplementary Table 1**).

Immunodetection. A tissue microarray containing two tissue cores (diameter 1.5mm) per CRC was constructed from FFPE tumor tissue blocks using the TMA Master (3DHISTECH Kft, Budapest, Hungary). Tonsil, sigmoid colon, and placental tissue were included as references. Regions of interest were selected on hematoxylin and eosin stains. A 4µm section was cut from the tissue microarray, deparaffinized, and rehydrated using xylene and decreasing ethanol concentrations. Heat-mediated antigen retrieval was achieved by boiling the section in sodium citrate (0.1M, pH 6), after which the section was incubated with Superblock solution (Thermo Fisher Scientific) to minimize non-specific antibody binding. Following washes in PBS (supplemented with 0.05% tween and 1% BSA), the section was incubated with antibody-metal conjugates using the conditions described in **Supplementary Table 1**.

Data acquisition. The Hyperion mass cytometry imaging system (Fluidigm) was autotuned using a 3-element tuning slide (Fluidigm), with a minimal detection of 1500 mean duals of 175Lu being required as an extra threshold for successful tuning. For each tissue core, an area of 1000x1000µm was ablated at 200Hz. Raw data was exported as MCD files and visualized with MCD viewer (Fluidigm).

Image enhancement, semi-automated background removal, and creation of single cell masks. MCD files were converted into tiff files using MCD viewer, following which images were enhanced (removal of outliers with values <1st or >99th percentile) using MATLAB (MathWorks, Natick, MA, USA). Ilastik's random forest classifier[44] was trained to distinguish background from real signal for every marker (exporting data as binary expression maps with background pixels set to 0 and real pixels set to 1) and to create probability masks for nuclei (based on DNA signal), tumor membranes (based on keratin signal) and stromal membranes (based on vimentin signal).[42] Using these probability masks, single-cell masks were created for all samples with CellProfiler[45], which were validated through visual comparison with the original IMC images.

Single-cell clustering and phenotype calling. Single-cell masks of each sample and binary expression maps of each marker were loaded into ImaCytE[46], in which the relative frequencies of positive pixels per cell were visualized and exported as single-cell FCS files. The latter were analyzed by t-distributed stochastic neighborhood embedding (t-SNE) in Cytosplore[47], in which Mean-shift clustering was used to group visual neighborhoods in the t-SNE embedding. The resulting groups were assigned a phenotype name based on the expression of lineage-specific markers (**Supplementary Table 2**) and were loaded back into ImaCytE for visual validation.

Multiplex immunofluorescence imaging

To further evaluate the immune cell phenotypes of interest as identified by IMC, we next applied mIF imaging using selected panels of antibodies on the entire set of tumors (**Supplementary Table 1**). For the assessment of T cells, simultaneous detection of CD4, CD8, CD103, granzyme B (GZMB), and PD-1 was applied, whereas a triple mIF panel targeting CD204, HLA-DR, and CD15 was used to evaluate myeloid cell infiltration.

Immunodetection. The process involved deparaffinization, endogenous peroxidase blocking, and heat-induced epitope retrieval steps akin to those described in the IHC procedure, using 4µm FFPE sections. Next, an Opal amplified detection process was applied. To minimize non-specific antibody binding, slides were incubated with Superblock solution. Primary antibody incubation lasted one hour, after which BrightVision Goat Anti-Mouse/Rabbit IgG HRP (Immunologic) was applied as the secondary antibody. After each antibody application, different Opal fluorophores (690, 650 620, 570, 520; Akoya Biosciences, Marlborough, MA, USA) were used to visualize multiple markers within the same tissue section. Microwave treatment was then conducted to remove primary and secondary antibodies and other non-specific staining and reduce tissue autofluorescence. Following each incubation period, slides were washed three times with a 0.05% Tween in PBS solution. An additional step involving DAPI incubation was carried out to stain the nuclei. Tissue slides were mounted using ProLong Gold Antifade Reagent (Cell Signaling Technologies, MA, USA). Tonsil slides were included as

negative controls. These were subjected to incubation with 1% bovine serum albumin (BSA)/PBS in place of the primary antibody.

Data acquisition. mIF images were captured using the Vectra 3.0 Automated Quantitative Pathology Imaging system (Akoya Biosciences). Whole slide scans for DAPI stains were performed at 4x magnification, and approximately four areas of interest were designated per sample using Phenochart Software (Akoya Biosciences). The multispectral images (MSIs) were obtained at 20x magnification, and spectral separation of dyes was carried out using the Inform Cell Analysis Software (Akoya Biosciences). The spectral library was created using single-stain mIF slides.

Phenotype calling and cell counting. The PENGUIN tool was employed for image normalization, rescaling all images and markers between 0 and 1.[48] Subsequently, a two-step denoising process was applied, wherein a minimal signal threshold was set for each marker, followed by percentile normalization. Cell segmentation masks were created from the normalized images using CellProfiler.[45] Initially, nuclei were defined using the DNA images, and membranes were added using the membrane markers from the dataset. For each cell outlined by CellProfiler, the mean intensity of each marker was calculated. Employing the FlowSOM R-package (version 2.6.0)[49], all cells were clustered based on mean marker intensity (FlowSOM settings: xdim = 5, ydim = 4, nClus = 5). Cluster evaluation involved visual inspection, with merging occurring for clusters exhibiting similar marker profiles and guided by prior knowledge of marker biology. The final clusters were remapped onto the images and validated by comparison with raw data.

Correlation with coding microsatellite mutations

To evaluate the potential influence of the molecular background on the infiltrating T cell levels, we correlated the T cell counts from the current study with the number of cMS mutations per tumor (max. 20 cMS tested per tumor). The latter data is considered to be a measure of the degree of MSI[50] and was obtained from Helderman et al.[37], where we focused on the same cohort of tumors.

Statistical analysis

Statistical analyses were conducted using RStudio (Team R, Integrated Development for R, Boston, MA, 2020). Continuous variables are expressed as mean (standard deviation, SD) or median (interquartile range, IQR) and were compared using either the (un)paired t-test or Mann-Whitney U test for two groups and the ordinary one-way ANOVA or Kruskal-Wallis test for more than two groups. Categorical variables are presented as proportions and were compared using Pearson's χ^2 test or Fisher's exact test for two categories, and Pearson's χ^2 test for more than two categories. Correlations were assessed using Pearson correlation. When applicable, raw *P* values were adjusted for the number of comparisons and outcomes using the Benjamini & Hochberg correction for multiple testing. All *P* values reported in this article are two-tailed and considered statistically significant at $P<0.05$. Cell counts were visualized in box and whisker plots displaying all data points (one point per tumor sample) and in heatmaps where phenotypes and MMR groups underwent unsupervised hierarchical clustering, using RStudio (Team R, Integrated Development for R, Boston, MA, 2020) and the ComplexHeatmap package.[51]

Results

An overview of the clinical and histological characteristics of each MMR group, encompassing 18 *MLH1*-, 16 *MSH2*-, 40 *MSH6*-, and 23 *PMS2*-mutated CRCs, along with 35 sporadic MMR-d CRCs due to *MLH1*-PM, is provided in **Supplementary Table 3**. A full description of all available clinical and histological characteristics for each analyzed CRC (including tumor IDs) is presented in **Supplementary Table 4**. Of note, *MSH6*-mutated CRCs were diagnosed at higher ages and more often located distally than other LS-associated CRCs.

Immune profiles are not specific to MMR mutations.

To examine the immune landscape of LS-associated CRCs, we initially applied a 40-marker IMC panel to eight tumor tissues per MMR group (with successful data acquisition for all but one *PMS2*-mutated CRC, tumor ID PMS2_08).[41] Based on this panel; we were able to identify five cancer, eleven lymphoid (including eight T cell phenotypes), seven myeloid, and four stromal cell phenotypes (**Supplementary Table 2**). The median cell count per MMR group for each identified phenotype through IMC is detailed in **Supplementary Table 5**.

Unsupervised hierarchical clustering of the IMC phenotypes did not identify clusters uniquely associated with selected MMR group(s), except for *MSH6*-mutated CRCs, which were generally characterized by a lower relative frequency of T cells (**Figure 1A**). In line with the latter, minor distinctions were observed in the levels of ($CD4^+$; $CD8^+$) T cells, which tended to be higher in *MLH1*-mutated CRCs, *MLH1*-PM CRCs, and a subset of *PMS2*-mutated CRCs compared to *MSH2*-mutated CRCs and *MSH6*-mutated CRCs (**Supplementary Figure 2**, **Supplementary Table 5**). A similar trend was noted for $CD8^+$ T cells expressing GZMB (a serine protease secreted by activated $CD8^+$ T cells[52]), PD-1 (an inhibitory checkpoint molecule expressed by activated/primed T cells[53]), and CD103 (a mediator of adhesion and tissue retention of $CD8^+$ T cells[54, 55]) (**Supplementary Figure 3**, **Supplementary Table 5**). In the myeloid cell compartment, granulocytes ($CD15^+$ cells) also appeared more prevalent in *MLH1*-mutated, *MLH1*-PM, and *PMS2*-mutated CRCs compared to *MSH2*- and *MSH6*-mutated CRCs

(**Supplementary Figure 2**, **Supplementary Table 5**). Conversely, the count of CD204$^+$ macrophages was slightly higher in *MSH2*-mutated CRCs (**Supplementary Figure 2**, **Supplementary Table 5**).

Based on the previous observations, we next applied targeted mIF and IHC with selected antibody panels on full slides of the entire set of tumors to validate the IMC results of the phenotypes discussed in the previous paragraph. The median cell count per MMR group for the phenotypes observed through mIF and IHC is presented in **Supplementary Table 6**.

Firstly, we evaluated CD4$^+$ and CD8$^+$ T cells, including their CD103/GZMB/PD-1 status, using mIF. Based on the mIF dataset, the median density of CD4$^+$ T cells (**Figure 1B**) and CD8$^+$ T cells (**Figure 1C**) was consistent across CRCs in each MMR group (**Figure 1D**). Similarly, the proportion of CD4$^+$ T cells and CD8$^+$ T cells expressing GZMB (**Figure 1E**), PD-1 (**Figure 1F**), and/or CD103 (**Figure 1G**) showed only modest variation between CRCs from each MMR group, thereby suggesting that T cell infiltration and activation does not seem to be influenced by a specific MMR defect.

Secondly, we analyzed CD204$^+$ macrophages and granulocytes through mIF. Similar to the lack of evident differences regarding the lymphoid phenotypes, we noted comparable levels of CD204$^+$ macrophage and granulocyte infiltration across CRCs in every MMR group (**Supplementary Figure 4**).

To determine if the comparable immune profiles of the different MMR groups observed through mIF were also mirrored by similar immune evasive events in various LS-associated CRCs, we next examined HLA class I and PD-L1 expression by IHC across the entire set of tumors. HLA class I defects were observed in 73% of all MMR-d CRCs (**Figure 2A**), consistent with previous studies.[9, 10] Total loss of HLA class I expression (absent membranous detection of both HCA2 and HC10 clones) was seen in 53% of cases, while partial loss (absent membranous detection of either HCA2 or HC10) was noted in 20% of cases. Among the CRCs with any HLA class I defect(s) (total or partial loss), aberrant β2M expression was seen less frequently (*P*=<0.001) in sporadic *MLH1*-PM CRCs (37%) versus hereditary *MLH1*- (85%), *MSH2*- (58%), *MSH6*- (70%) and *PMS2*-mutated (53%) CRCs (**Figure 2B**). PD-L1 expression could be

detected in tumor cells in a minority of *MLH1*-PM CRCs (20%), *MSH2*- (25%), *MSH6*- (17%), and *PMS2*-mutated (4%) CRCs, accounting for 8% of all CRCs (**Figure 2C**).

We then assessed the presence of γδ T cells (GD T cells; $CD3^+CD45^+GD^+$ cells) in the entire set of tumors through conventional IHC for the TCR δ [H-41] clone since γδ T cells were recently discovered to be involved in responses to immune checkpoint blockade in MMR-d CRCs with HLA class I defects[56]. As per the IMC data (**Supplementary Table 5**), γδ T cells were identified in varying degrees in CRCs from all MMR groups. IHC analysis of the entire cohort validated γδ T cells to be present in the majority (84%) of CRCs, with the median γδ T cell count being comparable in each MMR group (**Figure 3A-B**). The γδ T cell count did not associate with the tumors' HLA class I status (**Figure 3C**).

$CD8^+$ T cell levels negatively correlate with cMS mutations in *MLH1*-mutated CRCs

Finally, we correlated the T cell counts from the current study with the number of cMS mutations obtained from Helderman et al.[37] to evaluate the potential influence of the molecular background on the infiltrating T cell levels. Negative correlations were observed between the number of cMS mutations and the number of $CD4^+$ T cells (all $CD4^+$ T cell phenotypes combined) when considering all CRCs (Pearson's r -0.221; *P*=0.013) or when specifically considering *MLH1*-PM CRCs (Pearson's r -0.370; *P*=0.029) (**Figure 4A-B**, **Supplementary Figure 5**). Likewise, a negative correlation was identified between the number of cMS mutations and the number of $CD8^+$ T cells (all $CD8^+$ T cell phenotypes combined) when considering the *MLH1*-mutated CRCs only (Pearson's r -0.540; *P*=0.021) (**Figure 4C-D**, **Supplementary Figure 5**). The HLA class I status (total loss) was unaffected (*P*=0.125) by whether tumors had fewer than the median number (=13) of cMS mutations or equal to or more than the median number of cMS mutations.

Discussion

Recent studies have indicated variability in both the phenotype of LS carriers[22-30] and the genotype of LS-associated CRCs[31-37] based on the mutated MMR gene, including potential differences in the degree of microsatellite instability (i.e. number of insertion/deletion mutations at microsatellite regions), which appears to be lowest in *MSH6*-mutated CRCs.[36, 37] These studies have prompted the question of whether LS-associated CRCs also demonstrate diversity in immune profiles, which could potentially have implications with regard to immunotherapy management and cancer vaccine approaches and would strengthen the notion of considering LS as multiple gene-specific syndromes. However, comprehensive studies that quantitatively and qualitatively compare immune profiles of different MMR groups are scarce, applied relatively limited immunohistochemistry techniques (e.g., focusing on CD3+/CD8+ markers only) or included only a few *MSH6*- and *PMS2*-mutated CRCs.

Using IMC and mIF on one of the most extensive cohorts of LS-associated CRCs available for immunological assessment to date, our results challenge the idea that the immune profile of LS-associated CRCs depends on the specific underlying MMR defect. Instead, our findings reveal comparable immune profiles across CRCs from all MMR groups and variability within. This contrasts with our prior research, which showed lower T cell infiltration in *PMS2*-mutated CRCs compared to *MLH1*- and *MSH2*-mutated CRCs.[50] However, the current study surpasses our earlier work in sample size and the range of included immune markers. The comparable immune response towards CRCs from every MMR group suggests that all MMR-d CRCs, independent of the MMR defect, will display sensitivity to immune checkpoint blockade. Recent evidence supporting this notion includes pathological responses observed in 100% of MMR-d CRCs compared to only 27% of MMR-proficient CRCs following neoadjuvant ipilimumab (anti-CTLA-4) plus nivolumab (anti-PD-1) treatment.[19] However, it is noteworthy that current immunotherapy-related trials generally lack stratification of response by the MMR defect, potentially combining sporadic with hereditary tumors without specifying the underlying MMR defect.[15-19] Consequently, a crucial step would be to validate our hypothesis by stratifying current and future immunotherapy response data based on the MMR defect.

Additional findings with potential implications for immunotherapy response include the frequent loss of HLA class I and β2M expression and the presence of γδ T cells in most tumors across all MMR groups. The increased occurrence of aberrant β2M expression in hereditary versus sporadic MMR-d CRCs with HLA class I defects aligns with our prior observations, though our earlier research did not differentiate between MMR groups.[9, 10] This suggests that hereditary MMR-d CRCs follow distinct evolutionary pathways in tumorigenesis compared to sporadic MLH1-PM CRCs, regardless of the specific mutated MMR gene. Our current study found the prevalence of β2M defects ranging from 53% to 85%, depending on the MMR defect, which seems to exceed earlier findings of 17% to 51%.[9-11, 57-59] Additionally, these findings do not directly align with recently published *B2M* mutation data from *MSH6*-mutated CRCs in the same cohort, where only three out of the 22 genotyped *MSH6*-mutated CRCs displayed *B2M* mutations.[37] However, this discrepancy might be due to incomplete sequencing of the entire B2M gene in previous studies. The presence of γδ T cells, recently found to be enriched in tumors from patients with sporadic MMR-d CRCs following dual PD-1 and CTLA-4 blockade, may contribute to the immune checkpoint blockade response, particularly in patients with HLA class I-negative MMR-d CRCs, as their activation is not reliant on HLA class I binding.[56] Our study is the first to validate their presence in hereditary MMR-d CRCs.

The observed negative correlation between the quantity of infiltrating T cells and the number of cMS mutations per tumor, particularly pronounced in *MLH1*-mutated CRCs, may imply that the acquittance of immune evasion strategies is influenced by a greater mutational burden, possibly due to heightened selective pressure. Intriguingly, since the HLA class I status remained consistent regardless of the number of cMS mutations in a tumor, mechanisms other than the loss of HLA class I expression may be at the basis of this difference, which warrant attention in forthcoming immunological studies on LS-associated CRCs.

In conclusion, by employing high-dimensional immune profiling techniques on one of the most extensive LS-associated CRC cohorts documented to date, with a comprehensive representation of

MSH6- and *PMS2*-mutated CRCs, we illustrate that the immune profile of LS-associated CRCs remains consistent irrespective of the underlying MMR defect. This uniformity persists despite previously reported variations in the phenotype of LS carriers and the genotype of LS-associated CRCs, including varying degrees of MSI. These findings hold promise for immunotherapy strategies, suggesting sensitivity even in *MSH6*- and *PMS2*-mutated CRCs, and may contribute to a deeper understanding of the intricate interplay between tumors and the immune system in (MMR-d) CRCs and cancer in general.

References

1. Peltomaki P. Update on Lynch syndrome genomics. Fam Cancer. 2016;15(3):385-93.
2. Bohaumilitzky L, von Knebel Doeberitz M, Kloor M, et al. Implications of Hereditary Origin on the Immune Phenotype of Mismatch Repair-Deficient Cancers: Systematic Literature Review. J Clin Med. 2020;9(6).
3. Buckowitz A, Knaebel HP, Benner A, et al. Microsatellite instability in colorectal cancer is associated with local lymphocyte infiltration and low frequency of distant metastases. Br J Cancer. 2005;92(9):1746-53.
4. Dolcetti R, Viel A, Doglioni C, et al. High prevalence of activated intraepithelial cytotoxic T lymphocytes and increased neoplastic cell apoptosis in colorectal carcinomas with microsatellite instability. Am J Pathol. 1999;154(6):1805-13.
5. Kloor M, Staffa L, Ahadova A, et al. Clinical significance of microsatellite instability in colorectal cancer. Langenbecks Arch Surg. 2014;399(1):23-31.
6. Michael-Robinson JM, Biemer-Huttmann A, Purdie DM, et al. Tumour infiltrating lymphocytes and apoptosis are independent features in colorectal cancer stratified according to microsatellite instability status. Gut. 2001;48(3):360-6.
7. Shia J, Holck S, Depetris G, et al. Lynch syndrome-associated neoplasms: a discussion on histopathology and immunohistochemistry. Fam Cancer. 2013;12(2):241-60.
8. Smyrk TC, Watson P, Kaul K, et al. Tumor-infiltrating lymphocytes are a marker for microsatellite instability in colorectal carcinoma. Cancer. 2001;91(12):2417-22.
9. de Miranda NF, Goudkade D, Jordanova ES, et al. Infiltration of Lynch colorectal cancers by activated immune cells associates with early staging of the primary tumor and absence of lymph node metastases. Clin Cancer Res. 2012;18(5):1237-45.
10. Dierssen JW, de Miranda NF, Ferrone S, et al. HNPCC versus sporadic microsatellite-unstable colon cancers follow different routes toward loss of HLA class I expression. BMC Cancer. 2007;7:33.
11. Kloor M, Michel S, Buckowitz B, et al. Beta2-microglobulin mutations in microsatellite unstable colorectal tumors. Int J Cancer. 2007;121(2):454-8.
12. Kloor M, von Knebel Doeberitz M. The Immune Biology of Microsatellite-Unstable Cancer. Trends Cancer. 2016;2(3):121-33.
13. Ozcan M, Janikovits J, von Knebel Doeberitz M, et al. Complex pattern of immune evasion in MSI colorectal cancer. Oncoimmunology. 2018;7(7):e1445453.
14. Schwitalle Y, Kloor M, Eiermann S, et al. Immune response against frameshift-induced neopeptides in HNPCC patients and healthy HNPCC mutation carriers. Gastroenterology. 2008;134(4):988-97.
15. Benatti P, Gafa R, Barana D, et al. Microsatellite instability and colorectal cancer prognosis. Clin Cancer Res. 2005;11(23):8332-40.
16. Le DT, Durham JN, Smith KN, et al. Mismatch repair deficiency predicts response of solid tumors to PD-1 blockade. Science. 2017;357(6349):409-13.
17. Popat S, Hubner R, Houlston RS. Systematic review of microsatellite instability and colorectal cancer prognosis. J Clin Oncol. 2005;23(3):609-18.
18. Lenz HJ, Van Cutsem E, Luisa Limon M, et al. First-Line Nivolumab Plus Low-Dose Ipilimumab for Microsatellite Instability-High/Mismatch Repair-Deficient Metastatic Colorectal Cancer: The Phase II CheckMate 142 Study. J Clin Oncol. 2022;40(2):161-70.
19. Chalabi M, Fanchi LF, Dijkstra KK, et al. Neoadjuvant immunotherapy leads to pathological responses in MMR-proficient and MMR-deficient early-stage colon cancers. Nat Med. 2020;26(4):566-76.
20. Gebert J, Gelincik O, Oezcan-Wahlbrink M, et al. Recurrent Frameshift Neoantigen Vaccine Elicits Protective Immunity With Reduced Tumor Burden and Improved Overall Survival in a Lynch Syndrome Mouse Model. Gastroenterology. 2021;161(4):1288-302 e13.

21. Hernandez-Sanchez A, Grossman M, Yeung K, et al. Vaccines for immunoprevention of DNA mismatch repair deficient cancers. J Immunother Cancer. 2022;10(6).
22. Dominguez-Valentin M, Sampson JR, Seppala TT, et al. Cancer risks by gene, age, and gender in 6350 carriers of pathogenic mismatch repair variants: findings from the Prospective Lynch Syndrome Database. Genet Med. 2020;22(1):15-25.
23. Miyaki M, Konishi M, Tanaka K, et al. Germline mutation of MSH6 as the cause of hereditary nonpolyposis colorectal cancer. Nat Genet. 1997;17(3):271-2.
24. Moller P, Seppala T, Bernstein I, et al. Cancer incidence and survival in Lynch syndrome patients receiving colonoscopic and gynaecological surveillance: first report from the prospective Lynch syndrome database. Gut. 2017;66(3):464-72.
25. Moller P, Seppala TT, Bernstein I, et al. Cancer risk and survival in path_MMR carriers by gene and gender up to 75 years of age: a report from the Prospective Lynch Syndrome Database. Gut. 2018;67(7):1306-16.
26. Plaschke J, Engel C, Kruger S, et al. Lower incidence of colorectal cancer and later age of disease onset in 27 families with pathogenic MSH6 germline mutations compared with families with MLH1 or MSH2 mutations: the German Hereditary Nonpolyposis Colorectal Cancer Consortium. J Clin Oncol. 2004;22(22):4486-94.
27. Suerink M, Rodriguez-Girondo M, van der Klift HM, et al. An alternative approach to establishing unbiased colorectal cancer risk estimation in Lynch syndrome. Genet Med. 2019;21(12):2706-12.
28. Ten Broeke SW, van der Klift HM, Tops CMJ, et al. Cancer Risks for PMS2-Associated Lynch Syndrome. J Clin Oncol. 2018;36(29):2961-8.
29. Wagner A, Hendriks Y, Meijers-Heijboer EJ, et al. Atypical HNPCC owing to MSH6 germline mutations: analysis of a large Dutch pedigree. J Med Genet. 2001;38(5):318-22.
30. Dominguez-Valentin M, Haupt S, Seppala TT, et al. Mortality by age, gene and gender in carriers of pathogenic mismatch repair gene variants receiving surveillance for early cancer diagnosis and treatment: a report from the prospective Lynch syndrome database. EClinicalMedicine. 2023;58:101909.
31. Ahadova A, Gallon R, Gebert J, et al. Three molecular pathways model colorectal carcinogenesis in Lynch syndrome. Int J Cancer. 2018;143(1):139-50.
32. Ahadova A, Pfuderer PL, Ahtiainen M, et al. Distinct Mutational Profile of Lynch Syndrome Colorectal Cancers Diagnosed under Regular Colonoscopy Surveillance. J Clin Med. 2021;10(11).
33. Engel C, Ahadova A, Seppala TT, et al. Associations of Pathogenic Variants in MLH1, MSH2, and MSH6 With Risk of Colorectal Adenomas and Tumors and With Somatic Mutations in Patients With Lynch Syndrome. Gastroenterology. 2020;158(5):1326-33.
34. Helderman NC, Bajwa-Ten Broeke SW, Morreau H, et al. The diverse molecular profiles of lynch syndrome-associated colorectal cancers are (highly) dependent on underlying germline mismatch repair mutations. Crit Rev Oncol Hematol. 2021;163:103338.
35. Ten Broeke SW, van Bavel TC, Jansen AML, et al. Molecular Background of Colorectal Tumors From Patients With Lynch Syndrome Associated With Germline Variants in PMS2. Gastroenterology. 2018;155(3):844-51.
36. Helderman NC, van der Werf-'t Lam AS, group MSHt, et al. Molecular profile of MSH6-associated colorectal carcinomas shows distinct features from other Lynch syndrome-associated colorectal carcinomas. Gastroenterology. 2023.
37. Helderman NC, Strobel F, Bohaumilitzky L, et al. Lower degree of microsatellite instability in colorectal carcinomas from *MSH6*-associated Lynch syndrome patients. bioRxiv. 2024.
38. Valle L. Lynch Syndrome: A Single Hereditary Cancer Syndrome or Multiple Syndromes Defined by Different Mismatch Repair Genes? Gastroenterology. 2023;165(1):20-3.

39. Moller P, Seppala TT, Ahadova A, et al. Dominantly inherited micro-satellite instable cancer - the four Lynch syndromes - an EHTG, PLSD position statement. Hered Cancer Clin Pract. 2023;21(1):19.
40. Bankhead P, Loughrey MB, Fernandez JA, et al. QuPath: Open source software for digital pathology image analysis. Sci Rep. 2017;7(1):16878.
41. Ijsselsteijn ME, van der Breggen R, Farina Sarasqueta A, et al. A 40-Marker Panel for High Dimensional Characterization of Cancer Immune Microenvironments by Imaging Mass Cytometry. Front Immunol. 2019;10:2534.
42. Ijsselsteijn ME, Somarakis A, Lelieveldt BPF, et al. Semi-automated background removal limits data loss and normalizes imaging mass cytometry data. Cytometry A. 2021;99(12):1187-97.
43. Krop J, van der Zwan A, Ijsselsteijn ME, et al. Imaging mass cytometry reveals the prominent role of myeloid cells at the maternal-fetal interface. iScience. 2022;25(7):104648.
44. Berg S, Kutra D, Kroeger T, et al. ilastik: interactive machine learning for (bio)image analysis. Nat Methods. 2019;16(12):1226-32.
45. Carpenter AE, Jones TR, Lamprecht MR, et al. CellProfiler: image analysis software for identifying and quantifying cell phenotypes. Genome Biol. 2006;7(10):R100.
46. Somarakis A, Van Unen V, Koning F, et al. ImaCytE: Visual Exploration of Cellular Micro-Environments for Imaging Mass Cytometry Data. IEEE Trans Vis Comput Graph. 2021;27(1):98-110.
47. van Unen V, Hollt T, Pezzotti N, et al. Visual analysis of mass cytometry data by hierarchical stochastic neighbour embedding reveals rare cell types. Nat Commun. 2017;8(1):1740.
48. Sequeira AMI, M.E.; Rocha, M.; de Miranda, N.F.C.C. PENGUIN: A rapid and efficient image preprocessing tool for multiplexed spatial proteomics. bioRxiv. 2024.
49. Van Gassen S, Callebaut B, Van Helden MJ, et al. FlowSOM: Using self-organizing maps for visualization and interpretation of cytometry data. Cytometry A. 2015;87(7):636-45.
50. Bajwa-Ten Broeke SW, Ballhausen A, Ahadova A, et al. The coding microsatellite mutation profile of PMS2-deficient colorectal cancer. Exp Mol Pathol. 2021;122:104668.
51. Gu Z, Eils R, Schlesner M. Complex heatmaps reveal patterns and correlations in multidimensional genomic data. Bioinformatics. 2016;32(18):2847-9.
52. Nowacki TM, Kuerten S, Zhang W, et al. Granzyme B production distinguishes recently activated CD8(+) memory cells from resting memory cells. Cell Immunol. 2007;247(1):36-48.
53. Sharpe AH, Pauken KE. The diverse functions of the PD1 inhibitory pathway. Nat Rev Immunol. 2018;18(3):153-67.
54. Mueller SN, Mackay LK. Tissue-resident memory T cells: local specialists in immune defence. Nat Rev Immunol. 2016;16(2):79-89.
55. van den Bulk J, van der Ploeg M, Ijsselsteijn ME, et al. CD103 and CD39 coexpression identifies neoantigen-specific cytotoxic T cells in colorectal cancers with low mutation burden. J Immunother Cancer. 2023;11(2).
56. de Vries NL, van de Haar J, Veninga V, et al. gammadelta T cells are effectors of immunotherapy in cancers with HLA class I defects. Nature. 2023;613(7945):743-50.
57. Clendenning M, Huang A, Jayasekara H, et al. Somatic mutations of the coding microsatellites within the beta-2-microglobulin gene in mismatch repair-deficient colorectal cancers and adenomas. Fam Cancer. 2018;17(1):91-100.
58. Dierssen JW, de Miranda NF, Mulder A, et al. High-resolution analysis of HLA class I alterations in colorectal cancer. BMC Cancer. 2006;6:233.
59. Janikovits J, Muller M, Krzykalla J, et al. High numbers of PDCD1 (PD-1)-positive T cells and B2M mutations in microsatellite-unstable colorectal cancer. Oncoimmunology. 2018;7(2):e1390640.

Figure captions

Figure 1. Immune profiles are not specified by the MMR gene defect. [**A**] Unsupervised hierarchical clustering of the phenotypes identified through IMC revealed considerable heterogeneity amongst the CRCs, but did not identify clusters specifically associated with selected MMR group(s). The heatmap showcasing lymphoid cell phenotypes only features T cell phenotypes, excluding B cells, plasma cells/plasmablasts, and innate lymphoid cells. The tumor IDs are shown on the x-axis. The overall number of [**B**] $CD4^+$ T cells (all $CD4^+$ T cell phenotypes combined) and [**C**] $CD8^+$ T cells (all $CD8^+$ T cell phenotypes combined) did not differ between the MMR groups. [**D**] Illustrative IMC image showing detection of DNA (dark blue), CD8 (red), GZMB (green), PD-1 (yellow), and CD103 (light blue), along with an illustrative mIF image showing detection of DNA (dark blue), CD4 (yellow), CD8 (red), GZMB (green), PD-1 (purple), and CD103 (light blue). The proportion of $CD8^+$ T cells expressing [**C**] GZMB, [**D**] PD-1, and [**E**] CD103 did not vary between the MMR groups. Cell counts are visualized in box and whisker plots displaying all data points (one point per tumor sample). *CRC, colorectal cancer; GZMB, granzyme B; IMC, imaging mass cytometry; mIF, multiplex immunofluorescence; MLH1-PM, MLH1 promotor hypermethylation; MMR, mismatch repair; PD-1, programmed death 1.*

Figure 2. Frequent HLA class I defects in CRCs from all MMR groups. [**A**] Percentages of CRCs showing total loss (absent membranous detection of both HCA2 and HC10 clones) or partial loss (absent membranous detection of either HCA2 or HC10) of HLA class I expression per MMR group. [**B**] Percentage of CRCs with any HLA class I defect(s) (total or partial loss) showing aberrant β2M expression per MMR group. [**C**] Percentage of CRCs in which PD-L1 expression was detected, stratified by MMR group. Evaluation was performed by IHC. Stromal cell staining was used as internal positive control. *β2M, β2-microglobulin; HLA, human leukocyte antigen; IHC, immunohistochemistry; MLH1-PM, MLH1 promotor hypermethylation; MMR, mismatch repair; PD-L1, programmed death-ligand 1.*

Figure 3. γδ T cells are present in the majority of LS-associated CRCs independent of the MMR and HLA class I status. [**A**] The median number of γδ T cells was comparable between CRCs from every MMR group and [**B**] was independent of the HLA class I status (total loss [HCA2 and HC10]). [**C**]

Illustrative IHC image showing γδ T cells (indicated by arrows) in a *MSH6*-mutated CRC. *HLA, human leukocyte antigen; LS, Lynch syndrome; MMR, mismatch repair.*

Figure 4. Infiltrating CD8⁺ T cell levels negatively correlate with the number of cMS mutations in *MLH1*-mutated CRCs. Correlations between the number of cMS mutations (up to 20 cMS tested per tumor) and [**A**] the number of CD4⁺ T cells in all CRCs, [**B**] CD4⁺ T cells in *MLH1*-PM CRCs [B], [**C**] CD8⁺ T cells in all CRCs, [**D**] and CD8⁺ T cells in *MLH1*-mutated CRCs. cMS mutation data was obtained from Helderman et al.[37] *cMS, coding microsatellite; CRC, colorectal cancer; MLH1-PM, MLH1 promotor hypermethylation.*

Supplementary Figure 1. Scoring of HLA class I defects through IHC. Illustrative examples of tumors scored positive or negative for HCA2, HC10 and β2M. *β2M, B2-microglobulin; HLA, human leukocyte antigen; IHC, immunohistochemistry.*

Supplementary Figure 2. T cell and myeloid cell counts in the IMC dataset. The number of [**A**] T cells, [**B**] CD4⁺ T cells, [**C**] CD8⁺ T cells, [**D**] CD103⁺ T cells, [**E**] CD103⁺ CD4⁺ T cells, [**F**] CD103⁺ CD8⁺ T cells, [**G**] granulocytes, [**H**] CD204⁺ macrophages, and [**I**] CD204⁺ CD163⁺ macrophages per tumor, stratified by MMR group. *IMC, imaging mass cytometry; MMR, mismatch repair.*

Supplementary Figure 3. T cell condition marker expression per IMC phenotype. Proportion of T cells positive for [**A**] CD39, [**B**] CD103, [**C**] GZMB, [**D**] ICOS, [**E**] IDO, [**F**] Ki-67, [**G**] PD-1, [**H**] Tbet, [**I**] and VISTA for each T cell phenotype per MMR group, as evaluated by IMC. Dots represent the percentage of cells per sample (calculated based on two tissue cores per sample). Black bars represent the median percentage of cells per MMR mutation group. High percentages of CD103⁺ cells in the CD103⁺ T cells, CD103⁺CD4⁺ T cells and CD103⁺CD8⁺ T cells demonstrate that our Mean-shift clustering in Cytosplore was successfully conducted. *CRC, colorectal cancer; GZMB, granzyme B; IDO, indoleamine 2,3-dioxygenase, IMC, imaging mass cytometry; MLH1-PM, MLH1 promotor hypermethylation; MMR, mismatch repair; PD-1, programmed death 1.*

Supplementary Figure 4. Uniform myeloid cell compartments across MMR groups. The overall number of [**A**] (HLA-DR$^{-/+}$) CD204^{+} macrophages and [**B**] (HLA-DR$^{-/+}$) granulocytes did not differ between the MMR groups, as evaluated by mIF. *mIF, multiplex immunofluorescence; MMR, mismatch repair.*

Supplementary Figure 5. Correlation between the number of cMS mutations and infiltrating T cell levels per MMR group. Correlations between the number of cMS mutations (up to 20 cMS tested per tumor) and [**A-E**] the number of CD4^{+} T cells and [**F-J**] CD4^{+} T cells per tumor, stratified by MMR group. cMS mutation data was obtained from Helderman et al.[37] *cMS, coding microsatellite; CRC, colorectal cancer; MLH1-PM, MLH1 promotor hypermethylation.*

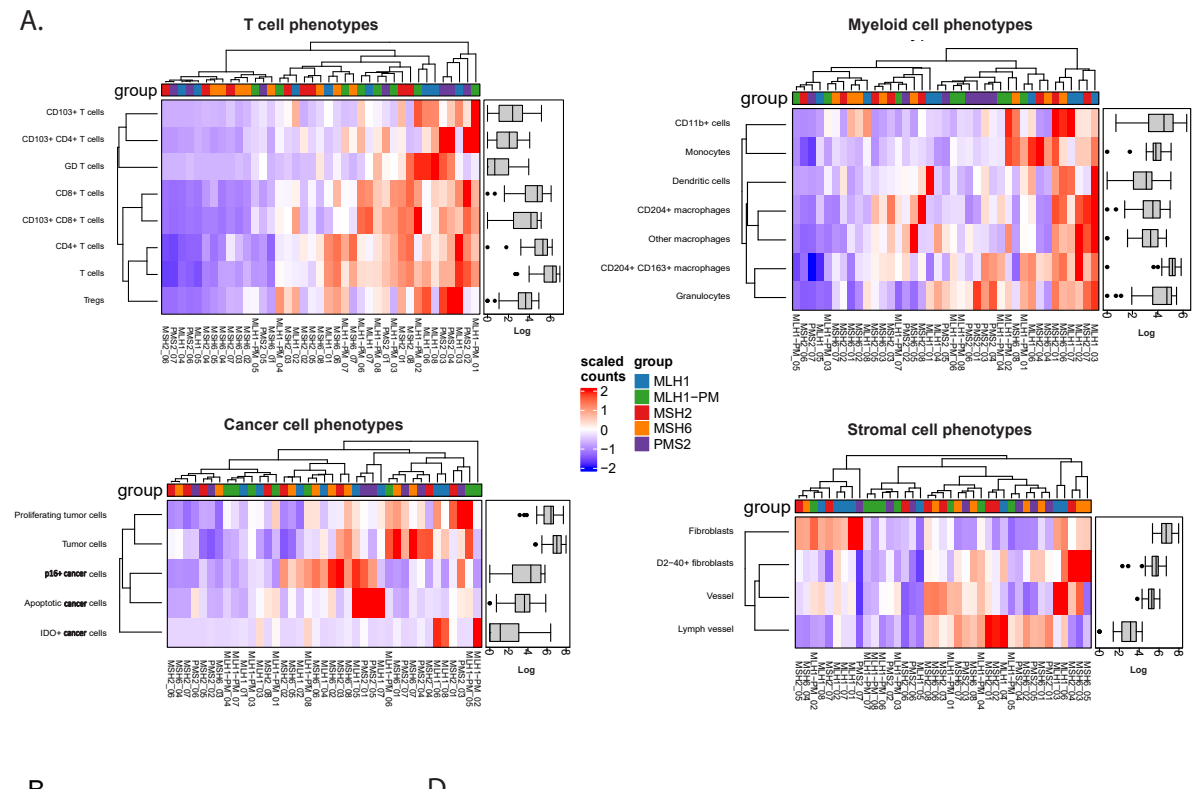
A.
T cell phenotypes
group
CD103+ T cells
CD103+ CD4+ T cells
GD T cells
CD8+ T cells
CD103+ CD8+ T cells
CD4+ T cells
T cells
Tregs
Log
Myeloid cell phenotypes
CD11b+ cells
Monocytes
Dendritic cells
CD204+ macrophages
Other macrophages
CD204+ CD163+ macrophages
Granulocytes
scaled counts
group
MLH1
MLH1−PM
MSH2
MSH6
PMS2
Cancer cell phenotypes
Proliferating tumor cells
Tumor cells
p16+ cancer cells
Apoptotic cancer cells
IDO+ cancer cells
Stromal cell phenotypes
Fibroblasts
D2−40+ fibroblasts
Vessel
Lymph vessel

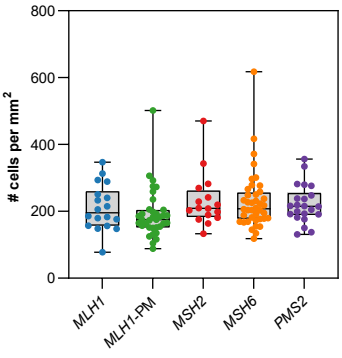
B.
Total CD4+ T cells
cells per mm2
MLH1
MLH1-PM
MSH2
MSH6
PMS2

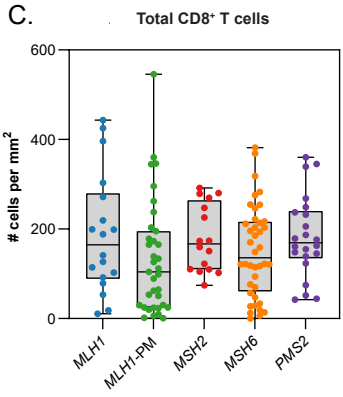
C.
Total CD8+ T cells
cells per mm2
MLH1
MLH1-PM
MSH2
MSH6
PMS2

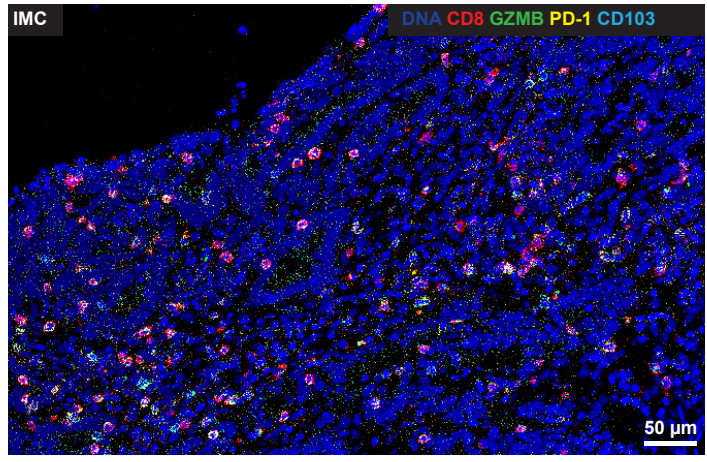
D.
IMC
DNA CD8 GZMB PD-1 CD103
50 µm

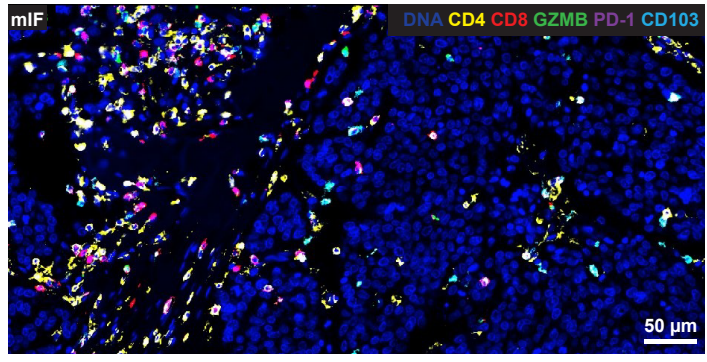
mIF
DNA CD4 CD8 GZMB PD-1 CD103
50 µm

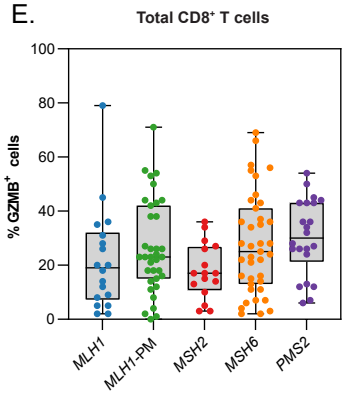
E.
Total CD8+ T cells
% GZMB+ cells
MLH1
MLH1-PM
MSH2
MSH6
PMS2

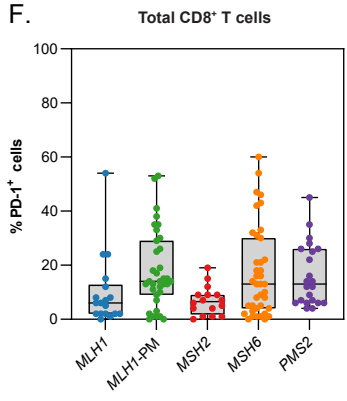
F.
Total CD8+ T cells
% PD-1+ cells
MLH1
MLH1-PM
MSH2
MSH6
PMS2

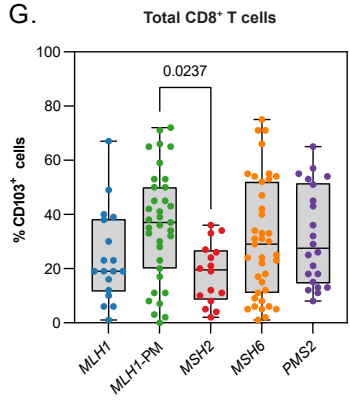
G.
Total CD8+ T cells
0.0237
% CD103+ cells
MLH1
MLH1-PM
MSH2
MSH6
PMS2

A.
% CRCs
100
50
0
MLH1
MLH1-PM
MSH2
MSH6
PMS2
HLA class I defect(s)
Total loss [HCA2 and HC10]
Partial loss [HCA2 or HC10]
No loss
Unknown
B.
% CRCs with any HLA class I defect(s)
β2M defect
Yes
No
Unknown
C.
% CRCs
PD-L1 expression
Yes
Yes, but limited compared to stroma
No
Unknown

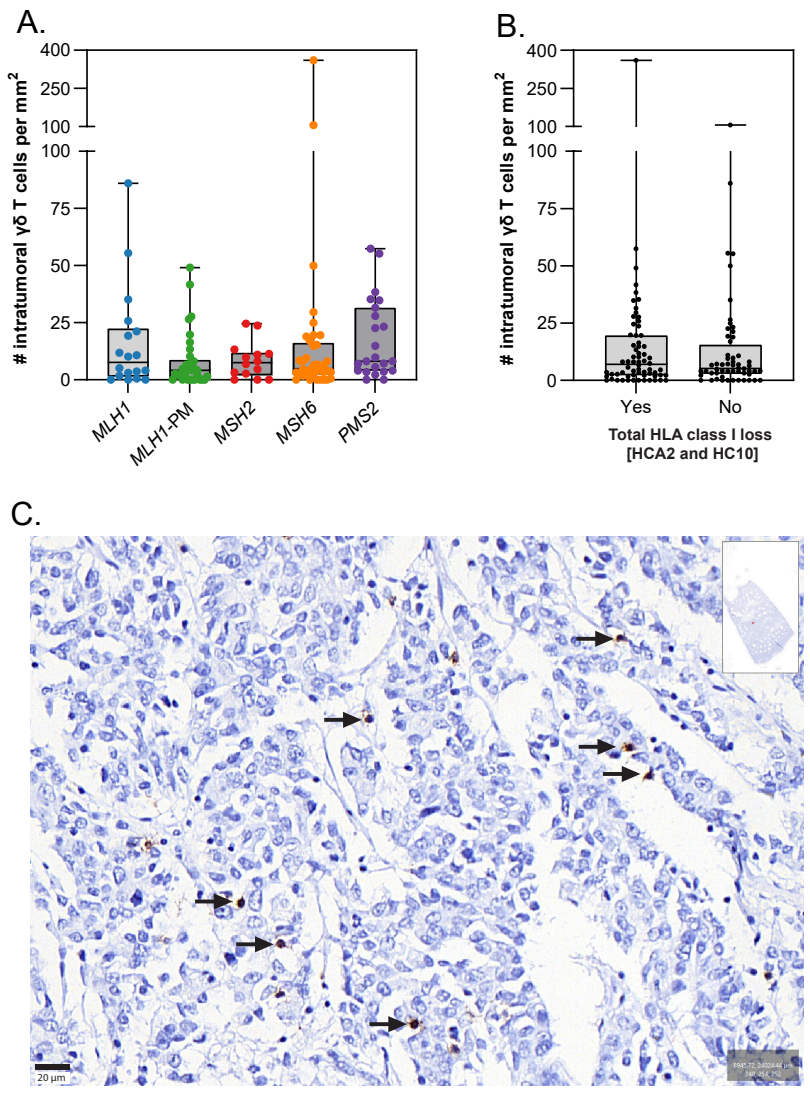
A.
intratumoral γδ T cells per mm²
400
250
100
100
75
50
25
0
MLH1
MLH1-PM
MSH2
MSH6
PMS2
B.
intratumoral γδ T cells per mm²
400
250
100
100
75
50
25
0
Yes
No
Total HLA class I loss
[HCA2 and HC10]
C.
20 µm

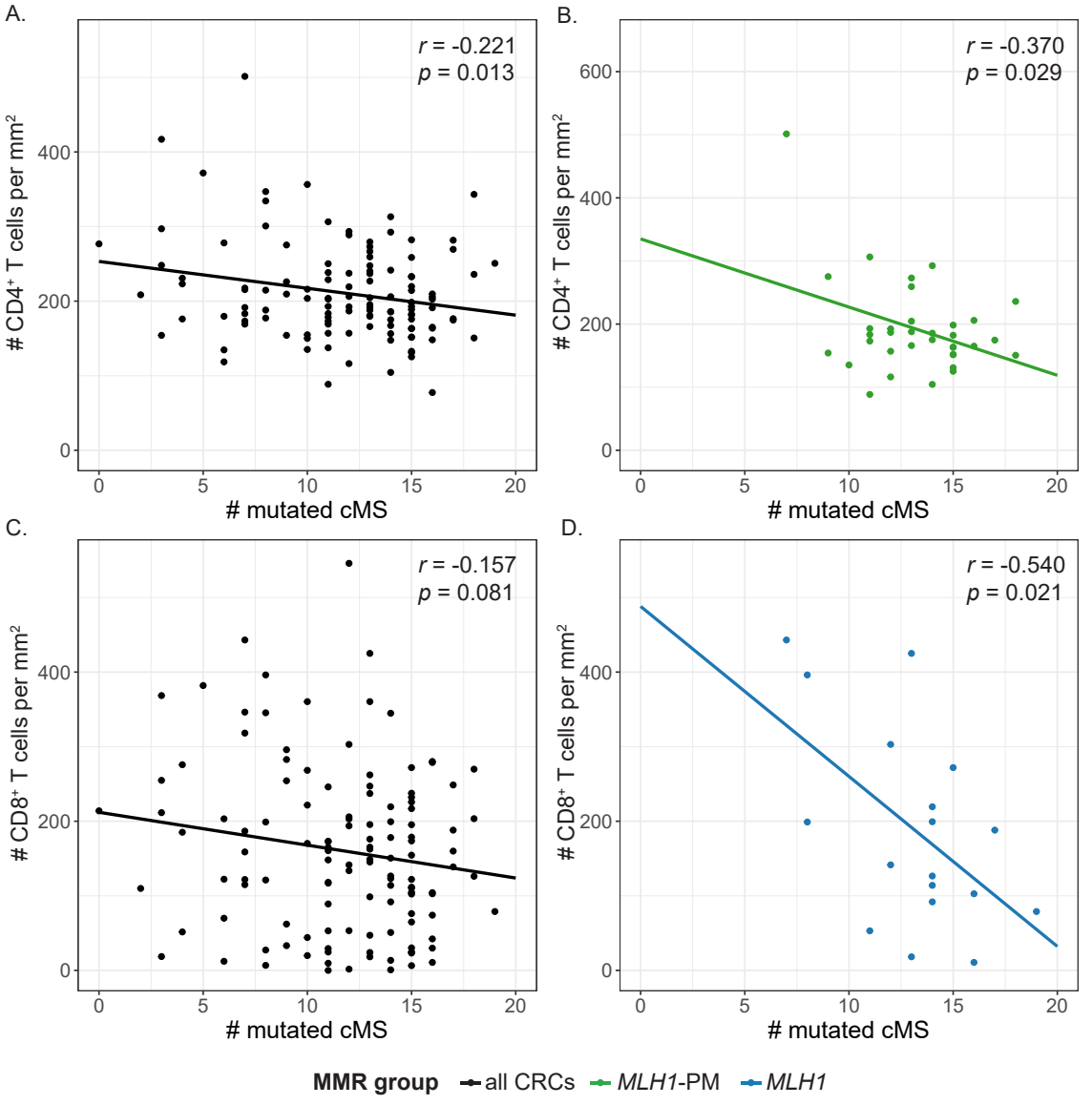
A.
r = -0.221
p = 0.013
# CD4+ T cells per mm2
# mutated cMS
B.
r = -0.370
p = 0.029
# CD4+ T cells per mm2
# mutated cMS
C.
r = -0.157
p = 0.081
# CD8+ T cells per mm2
# mutated cMS
D.
r = -0.540
p = 0.021
# CD8+ T cells per mm2
# mutated cMS
MMR group
all CRCs
MLH1-PM
MLH1